NIH Public Access
Author Manuscript
*Chem Mater*. Author manuscript; available in PMC 2009 November 11.

Published in final edited form as:
*Chem Mater*. 2008 November 11; 20(21): 6643–6656. doi:10.1021/cm801387z.

# Morphological and Phase Controlled Tungsten Based Nanoparticles: Synthesis and Characterization of Scheelites, Wolframites, and Oxides Nanomaterials

**Bernadette A. Hernandez-Sanchez**,
Sandia National Laboratories, Advanced Materials Laboratory, 1001 University Boulevard Southeast Albuquerque, NM 87106

**Timothy J. Boyle***,
Sandia National Laboratories, Advanced Materials Laboratory, 1001 University Boulevard Southeast Albuquerque, NM 87106

**Harry D. Pratt III**,
Sandia National Laboratories, Advanced Materials Laboratory, 1001 University Boulevard Southeast Albuquerque, NM 87106

**Mark A. Rodriguez**,
Sandia National Laboratories, Advanced Materials Laboratory, 1001 University Boulevard Southeast Albuquerque, NM 87106

**Luke N. Brewer**, and
Sandia National Laboratories, Advanced Materials Laboratory, 1001 University Boulevard Southeast Albuquerque, NM 87106

**Darren R. Dunphy**
The University of New Mexico, Department of Chemical Engineering, Albuquerque, New Mexico 87131

## Abstract

For the first time tungsten based nanoparticles (WNPs) of scheelite ($MWO_4$; M = Ca, Sr, Ba, Pb), wolframite ($MWO_4$; M = Mn, Fe, Zn & $(Mg_{0.60}Mn_{0.17}Fe_{0.26})WO_4$), and the oxide ($WO_3$ and $W_{18}O_{49}$) were synthesized from solution precipitation (i.e.,trioctylamine or oleic acid) and solvothermal (i.e., benzyl alcohol) routes. The resultant WNPs were prepared directly from tungsten (VI) ethoxide ($W(OCH_2CH_3)_6$, **1**) and stoichiometeric mixtures of the following precursors: $[Ca(N(SiMe_3)_2)_2]_2$ (**2**), $Pb(N(SiMe_3)_2)_2$ (**3**), $Mn[(\mu\text{-Mes})_2Mn(Mes)]_2$ (**4**), $[Fe(\mu\text{-Mes})(Mes)]_2$ (**5**), $Fe(CO)_5$ (**6**), $H^+[Ba_2(\mu_3\text{-ONep})(\mu\text{-ONep})_2(ONep)(ONep)_3(py)]^-_2$ (**7**), $H^+[Sr_5(\mu_4\text{-O})(\mu_3\text{-ONep})_4(\mu\text{-ONep})_4(ONep)(py)_4]^-$ (**8**), and $[Zn(Et)(ONep)(py)]_2$ (**9**) where Mes = $C_6H_2(CH_3)_3$-2,4,6, ONep = $OCH_2CMe_3$, Et = $CH_2CH_3$, and py = pyridine. Through these routes, the WNP morphologies were found to be manipulated by the processing conditions, while precursor selection influenced the final phase observed. For the solution precipitation route, **1** yielded (5 × 100 nm) $W_{18}O_{49}$ rods while stochiometeric reactions between **1** and (**2** – **9**) generated homogenous sub 30 nm nano-dots, -diamonds, -rods, and -wires for the $MWO_4$ systems. For the solvothermal route, **1** was found to produce wires of $WO_3$ with aspect ratios of 20 while (**1** & **2**) formed 10 – 60 nm $CaWO_4$ nanodots. Room temperature photoluminescent (PL) emission properties of select WNPs were also examined with fluorescence spectroscopy ($\lambda_{ex}$ = 320 nm). Broad PL emissions = 430, 420, 395, 420 nm were

*Author to whom correspondences should be sent: phone (505) 272-7625; fax (505) 272-7336; e-mail: tjboyle@sandia.gov.

NIH-PA Author Manuscript
NIH-PA Author Manuscript
NIH-PA Author Manuscript

NIH-PA Author Manuscript

NIH-PA Author Manuscript

NIH-PA Author Manuscript

noted for 5 × 100 nm $W_{18}O_{49}$ rods, 5 × 15 nm, $CaWO_4$ rods, 10 – 30 nm $CaWO_4$ dots, and 10 nm $BaWO_4$ diamonds, respectively.

## Introduction

There is little precedent for the use of solution route strategies that yield controlled morphologies of tungsten based nanoparticles (WNP), such as the metal tungstates ($MWO_4$) [i.e., scheelite ($CaWO_4$), wolframite ($(Mn,Fe)WO_4$)] or the simple tungsten oxides ($WO_x$). Solvothermal (SOLVO) and hydrothermal routes to $MWO_4$ that react commercially available $Na_2WO_4{\cdot}H_2O$ with metal halides,[1–11] -acetates,[12–16] -nitrates,[8,9,17,18] and -sulfates[11] have provided a glimpse of the possible controlled WNPs that can be produced through judicious choice of processing and precursor selection. As for the $WO_x$, only a handful of solution precipitation (SPPT) routes have been developed based on tungsten hexacarbonyl ($W(CO)_6$)[19,20] and tungsten(IV) chloride ($WCl_4$).[21,22] The data presented in these reports indicated that the final WNP properties was influenced by the crystallization temperature and solvents used during the SPPT process. None-the-less, the fundamental development of synthetic pathways that allow for the generation of tailored WNP is still being sought since control over the morphology and phase is critical for WNP's use in a number of diverse energy and sensor applications, such as: solid state lightning, bio-imaging, scintillators, humidity sensors, batteries, and catalysts.[6,11,19,23]

We are interested in using WNP for bio-imaging and sensing applications, which necessitates the development of controlled morphological 10 – 30 nm $MWO_4$ materials. In order to realize this goal, a general SPPT route that employed metal alkoxides ($M(OR)_x$) was sought. The continued interest in $M(OR)_x$ precursors stems from the fact that they possess an easily manipulated ligand set which offers greater control over the final nanomaterials than other systems. The ease of manipulation of this family of compounds has allowed us to formulate the "precursor structure affect" for controlled nano-morphology in a number of nanoceramic systems[23–25] as well as the "precursor decomposition pathway" for influencing the final crystalline phase.[24,25] Previous reports that employ $M(OR)_x$ for the preparation of even the simple $WO_x$ nanomaterials were surprisingly limited, but promising in terms of morphological control.[26,27] $WO_x$ nanorods were successfully synthesized from tungsten alkoxide ($W(OR)_6$) precursors (tungsten(VI) *iso*-propoxide ($W(OPr^i)_6$)[27] and tungsten(VI) oxo methoxide ($WO(OMe)_4$)[26]), in a benzyl alcohol SPPT route and in a study of "reactions under autogenic pressure at elevated temperature", respectively. Unfortunately, these methods required high temperatures (700 °C) or needed additional calcinations procedures to form $WO_3$. In addition to the limited references concerning the use of $W(OR)_x$, reports of WNP synthesized from metal amides ($M(NR_2)$) or metal alkyls ($MR_x$) which have also shown great efficacy in both SPPT and SOLVO routes to ceramic nanomaterials have not been reporte.[23,24,28]

For this investigation, we focused on exploiting the precursor structure decomposition phenomena associated with these neglected $M(OR)_x$ precursors to decipher the key variables for the production of tailored WNP nanomaterials. We also compared the reactivity and decomposition of $M(NR_2)_x$, $MR_x$, and $M(CO)_x$ in a newly developed SPPT routes that offer control over the final WNPs. These precursors have several advantages over the more commonly employed halides and nitrates including high solubility, high volatility, low decomposition temperatures, and condensation control that can be invoked through judicious manipulation of the ligand set. These tailored precursors allow for specific properties in the final materials to be fine-tuned. Following this approach enabled the development of a SPPT route to high yields of scheelite and wolframite nanomaterials, which to our knowledge has not been previously reported. In addition, a selection of $M(OR)_x$ and $M(NR_2)_x$ precursors have been studied using a SOLVO route. Both $MWO_4$ and $WO_x$ nanomaterials were prepared using

NIH-PA Author Manuscript

NIH-PA Author Manuscript

NIH-PA Author Manuscript

the commercially available tungsten(VI) ethoxide ($W(OEt)_6$, **1**) and stoichiometric mixtures of the following precursors in both SPPT and SOLVO routes: $[Ca(N(SiMe_3)_2)_2]_2$ (**2**), $Pb(N(SiMe_3)_2)_2$ (**3**), $Mn[(\mu\text{-Mes})_2Mn(Mes)]_2$ (**4**), $[Fe(\mu\text{-Mes})(Mes)]_2$ (**5**), $Fe(CO)_5$ (**6**), $H^+[Ba_2(\mu_3\text{-ONep})(\mu\text{-ONep})_2(ONep)(ONep)_3(py)]^-_2$ (**7**), and $H^+[Sr_5(\mu_4\text{-O})(\mu_3\text{-ONep})_4(\mu\text{-ONep})_4(ONep)(py)_4]^-$ (**8**), and $[Zn(ONep)(Et)(py)]_2$ (**9**) where, Mes = $C_6H_2(CH_3)_3$-2,4,6, ONep = $OCH_2CMe_3$, Et = $CH_2CH_3$, and py = pyridine. These precursors were easily introduced into both routes and produced WNPs with controlled properties. The details of their synthesis and characterization are discussed below.

## Experimental

All compounds described below were handled with rigorous exclusion of air and water using standard Schlenk line and glovebox techniques. The following chemicals were used as received and were stored under argon: Alfa Aesar: **1**; Aldrich: iron pentacarbonyl ($Fe(CO)_5$) (**6**), *neo*-pentanol (HONep), Sr°, Ba°, $CaI_2$, $PbBr_2$, $MnBr_2$, $FeBr_2$, $KN(Si(CH_3)_3)_2$, MgBrMes (1.0 M in THF), diethyl zinc ($ZnEt_2$) (1.0 M in hexanes), benzyl alcohol (BzOH), trioctylamine (TOA), oleic acid (OA), chloroform ($CHCl_3$), toluene (tol), pyridine (py), tetrahydrofuran (THF), and ethanol (EtOH). Solvents used to synthesize the precursors were obtained in Sure/Seal ™ bottles and stored under an argon atmosphere. The following compounds were synthesized according to published procedures: **2**[24,29,30], **3**[31], **4**[32], **5**[33], **7**[28,34], **8**[35], and **9**[25].

### General Synthesis of WNPs

A general description of both synthetic routes is first presented, followed by the complete experimental details and observations noted for each WNP synthesized. Two synthetic routes (a) SPPT and (b) SOLVO were used to synthesize $WO_x$, $MWO_4$ (M = Ca, Sr, Ba, Pb, Mn, Fe, Zn), and $(Fe,Mn)WO_4$ ceramic nanoparticles from stoichiometric mixtures of commercially available **1** with **2** – **9**, respectively.

**(a) SPPT—**A mixture of TOA/OA[36] (4.9 g, 13 mmol/1.8 g, 6.3 mmol) was placed in a three-neck round bottom flask equipped with a reflux condenser, septum, and thermocouple. Stoichiometric mixtures, of **1** with **2** – **9**, respectively, were added to the TOA/OA solution at room temperature under flowing argon. The solution was heated (~100 °C) and a clear orange or brown solution formed before undergoing a final color change and the formation of a precipitate (245–380 °C). After reaching the desired temperatures, the heating source was removed and the solutions were allowed to cool to room temperature. The WNPs were isolated by extraction with $CHCl_3$ followed by precipitation through the addition of ethanol (EtOH). The WNP precipitate was collected by centrifugation and rinsed with EtOH a second time before being dispersed again with $CHCl_3$ or toluene. *Note: over time, wire-like morphologies were observed to settle out of the dispersing solutions*.

**(b) SOLVO—**In the glove box, stoichiometric mixtures of **1**–**2** were dissolved in ~15 mL of BzOH and the clear solutions were transferred to the Teflon™ lined 45 mL Parr acid digestion bomb. The bomb was taken out of the glove box and placed in a furnace and was heated to 200 °C for 48 hrs at a rate of 10 °C/min. After this time, the bomb was cooled back to 24 °C at 10 °C/min. After cooling to room temperature, the WNP precipitate was collected by centrifugation and rinsed twice with EtOH.

### SPPT Experimental

**$W_{18}O_{49}$:** Used **1** (1.6 g, 3.6 mmol). Heating the solution to 100 °C formed a clear brown solution that changed to clear blue-green as the temperature increased. A dark blue precipitate occurred at 310 °C. The reaction was held at this temperature for 10 min. before cooling to room temperature. Percent Yield: 0.48 g (58.5%)

NIH-PA Author Manuscript

NIH-PA Author Manuscript

NIH-PA Author Manuscript

**$CaWO_4$:** Heating a mixture of **2** (0.54 g, 1.5 mmol) and **1** (0.68 g, 1.5 mmol) to 100 °C formed a clear brown solution that turned clear blue-green as the temperature increased (~200 °C). A blue-green precipitate occurred at 276 °C. The reaction was held at 276 °C for 1 min. before cooling to room temperature. Percent Yield: 0.18 g (41.9 %)

**$SrWO_4$:** Heating a mixture of **8** (0.46 g, 1.5 mmol) and **1** (0.68 g, 1.5 mmol) to 100 °C formed a clear orange solution that turned clear blue-green as the temperature increased (~200 °C). A blue-green precipitate occurred at 367 °C. The reaction was held at 367 °C for 2 min. before cooling to room temperature. Percent Yield: 0.39 g (77.3%)

**$BaWO_4$:** Heating a mixture of **7** (0.72 g, 1.5 mmol) and **1** (0.68 g, 1.5 mmol) to 100 °C formed a clear orange solution that turned clear yellow as the temperature increased (~200 °C). A white precipitate occurred at 356 °C. The reaction was heated to 362 °C and held for 1 min. before cooling to room temperature. Percent Yield: 0.24 g (41.5 %)

**$PbWO_4$:** Heating a mixture of **3** (0.79 g, 1.5 mmol) and **1** (0.68 g, 1.5 mmol) to 100 °C formed a clear brown solution that turned clear blue as the temperature increased (~250 °C).A light blue precipitate occurred at 356 °C. The reaction was heated to 362 °C and held for 15 min. before cooling to room temperature. Percent Yield: not calculated, mixed phase product

**$(Fe_{0.25}Mn_{0.75})WO_4$:** Heating a mixture of **4** (0.18 g, 0.55 mmol), **5** (0.052 g, 0.18 mmol), and **1** (0.33 g, 0.73 mmol) to 100 °C formed a clear orange solution that turned dark blue as the temperature increased (~270 °C). A brown precipitate occurred at 386 °C and the reaction was held at 386 °C for 10 min. before cooling to room temperature. Percent Yield: Mg impurity prevented accurate calculation.

**$MnWO_4$:** Heating a mixture of **4** (0.49 g, 1.5 mmol) and **1** (0.68 g, 1.5 mmol) to 100 °C formed a clear orange solution that turned dark green as the temperature increased (~200 °C). A light blue precipitate occurred at 375 °C. The reaction was held at 375 °C for 10 min. before cooling to room temperature. Percent Yield: not calculated, mixed phase product.

**$FeWO_4$:** Heating a mixture of **5** (0.75 g, 1.5 mmol) and **1** (0.68 g, 1.5 mmol) to 100 °C formed a clear orange solution that turned dark blue as the temperature increased (~270 °C) and then to brown at 351 °C. A light brown precipitation occurred at 380 °C. The reaction was held at 380 °C for 10 min. before cooling to room temperature. Percent Yield: not calculated, mixed phase product.

**$FeWO_4$:** Heating a mixture **6** (0.29 g, 1.5 mmol) and **1** (0.68 g, 1.5 mmol) to 100 °C formed a clear orange solution that turned black as the temperature increased (~180 °C) and then dark blue at 230 °C. A dark brown precipitation occurred at 330 °C. The reaction was held at 330 °C for 10 min. before cooling to room temperature. Percent Yield: 0.29 (63.0%)

**$ZnWO_4$:** Heating the mixture of **9** (0.39 g, 1.5 mmol) and **1** (0.68 g, 1.5 mmol) to 100 °C formed a clear orange solution that turned dark green as the temperature increased (~200 °C) and then to blue at 250 °C. A light blue precipitation occurred at 340 °C. The reaction was held at 340 °C for 10 min. before cooling to room temperature. Percent Yield: not calculated mixed, phase product.

### SOLVO Experimental

**$WO_3$:** Dissolved **1** (0.20 g, 0.44 mmol) in BzOH (15 mL) to form a clear orange solution. A blue precipitate and clear orange mother liquor was collected after cooling to room temperature. Percent Yield: not calculated mixed, phase.

NIH-PA Author Manuscript

NIH-PA Author Manuscript

NIH-PA Author Manuscript

**$CaWO_4$:** Dissolved **1** (0.20 g, 0.44 mmol) and **2** (0.16 g, 0.44 mmol) in BzOH (15 mL) to form a clear orange solution. A white precipitate and clear yellow mother liquor was collected after cooling to room temperature. Percent Yield: not calculated mixed, phase product.

### Powder X-ray Diffraction (PXRD)

Dried and washed WNP powders were mounted directly onto a Si zero background holder purchased from the Gem Dugout. Phase identification for the nanoscale materials was determined PXRD patterns collected on a PANalytical powder diffractometer employing Cu $K_\alpha$ radiation (1.5406 Å) and a RTMS X'Celerator detector. Samples were scanned at a rate of 0.02°/2 sec in the 2θ range of 10–;100°.

### Photoluminescence

The photoluminescence (PL) emission of select scheelites and $WO_x$ were examined at room temperature using a Fluorolog-3 Model FL3-21 from Horiba Jobin Yvon. Solutions of washed WNP particles prepared from SOLVO were dispersed in EtOH. WNPs prepared by SPPT were dispersed in $CHCl_3$, tol, or THF. An excitation wavelength ($\lambda_{ex}$= 320 nm) was used to obtain the emission spectra detected in the 350–;600 nm range. The emission spectra were corrected for non-uniform responses of the photomultiplier tube and the grating inside the emission monochromator.

### Transmission Electron Microscopy (TEM)

An aliquot of the particles dispersed in EtOH (SOLVO) or $CHCl_3$ (SPPT) was placed directly onto a lacy carbon Type-A, 300 mesh, copper TEM grid purchased from Ted Pella, Inc. The aliquot was then allowed to dry overnight. The resultant particles were studied using two instruments: the Philips CM 30 TEM with the Thermo Noran System Six Energy Dispersive X-ray (EDX) System and FEI Tecnai TF30 TEM/STEM with the EDAX EDX System, both operating at 300 kV accelerating voltage.

### Scanning Electron Microscopy (SEM)

The samples were dispersed onto carbon tape and coated with gold palladium using an Edwards sputter coater. Samples were imaged using a Zeiss Supra 55VP field emitter gun scanning electron microscope (FEGSEM). A Noran EDS detector and Noran System Six software was used for the acquisition of EDS spectra.

### Inductively Coupled Plasma Mass Spectroscopy (ICP-MS)

Molar ratios of the solid solution $(Fe_{0.60}Mn_{0.17}Mg_{0.26})WO_4$ were determined by digesting 0.10 g of the nanoparticles in 5 mL of high purity hydrochloric acid and 5 mL of deionized water (DI $H_2O$) at 70 °C. The solution was cooled to room temperature, diluted with DI $H_2O$, and then analyzed with a Perkin Elmer Elan 6100 ICP-MS to determine the elemental molar ratios.

## Results and Discussion

As mentioned previously, the properties of W-based systems depend critically on the phase and composition of the various components. For example, the simple $WO_x$ species are a main component of catalyst systems, lithium batteries, photo- and electrochromics, and gas sensors.[19,22] Their desirable bulk optic and electronic properties used for these applications arise from $WO_6$ octahedra packing arrangements and stoichiometery.[37,38] For bulk $MWO_4$, the W coordination chemistry has also been shown to dictate the fluorescent, magnetic, catalytic, and electronic properties.[11,39,40] The $MWO_4$ are categorized by the W-O coordination that is influenced by the divalent ionic ($M^{2+}$) radii size, where the scheelites (large $M^{2+}$) have

NIH-PA Author Manuscript

NIH-PA Author Manuscript

NIH-PA Author Manuscript

tetrahedral coordination and the wolframites (small $M^{2+}$ radii) adopt octahedral coordination. Because the crystal chemistry is so influential on the final bulk materials properties, it is important to investigate how the selection of precursor (i.e., $M(OR)_x$, $M(NR_2)_x$, and $M(R)_x$) will effect the final WNPs' phase.

Current WNP synthetic methods (i.e., SOLVO, hydrothermal) have had varied success in producing controlled morphologies.[1–3,5–11,13–15,18,41–44] Although a number of unique morphologies have been synthesized, there are few examples of <30 nm WNP and little is known about the fluorescent and electronic behavior in this size regime. In order to understand the WNP nanocrystal-structure property relationships of sub 30 nm particles, we have chosen to investigate a SPPT strategy to synthesize these nanomaterials. Recently SPPT routes, with various amines and carboxylic acids solvents, were used to synthesize transition metal oxides ($W_{18}O_{49}$, MnO, FeO)[19,36,45] and perovskites ($A^ETiO_3$, $A^E$ = Sr, Ba)[46], through the thermal decomposition of metal acetates, carbonyls, and non-crystallographically characterized $A^ETi(OR)_6$ alkoxides. Here, we investigated the combination of trioctylamine and oleic acid (TOA/OA) for our SPPT route in order to synthesize WNPs. It was determined that commercially available **1** produced $WO_x$ while stoichiometeric ratios of **1** and the following precursors: $M(NR_2)_x$ **2** – **3**, $MR_x$ **4** – **6**, and ONep derivatives **7** – **9** produced $MWO_4$. Discussion of the synthetic process follows for: (i) solution precipitation – scheelite; wolframite; oxide and (ii) solvothermal routes – scheelite; oxide. Table 1 summarizes the reaction products isolated as well as the effect of precursor and processing conditions on the final WNP properties.

## SPPT Synthesis of Scheelite WNPs

Using the SPPT route (TOA/OA), we undertook the synthesis of $MWO_4$ (M = Ca, Sr, Ba, Pb) nanoparticles using stoichiometric amounts of (**1** & **2**), (**1** & **8**), (**1** & **7**), or (**1** & **3**), respectively. The PXRD patterns for these WNPs are presented in Figure 1a–d. Phase pure tetragonal patterns, Figures 1a– c, were observed and indexed to scheelites: $CaWO_4$ (PDF # 41-1431)[47], $SrWO_4$ (PDF # 08-0490)[47], and $BaWO_4$ (PDF # 43-0646)[47], respectively. However, under the conditions used, the reaction between (**1** & **3**) formed a precipitate containing two phases that were indexed to the tetragonal phase of $PbWO_4$ stolzite (Figure 1d), (PDF # 19-0708)[47] and a secondary phase centered at 24.5 ° (2θ) assigned to a tungsten suboxide $W_{24}O_{68}$. This assignment is tenuous because the secondary phase's reflections are weak, broad, and remaining $W_{24}O_{68}$ peaks are coincidental with the stronger $PbWO_4$ reflections. Formation of $W_{24}O_{68}$ under the reaction conditions used for $PbWO_4$ may have resulted from Pb's volatility. Future synthetic reaction that utilize **3** will have a 5–10% augmentation (based on sol-gel template generated $PbTiO_3$ nanotubes) to account for this characteristic Pb loss.[48] The resulting PXRD data for all the reaction products obtained confirmed that the precursors and conditions used in the SPPT route to synthesize the scheelites were successful in producing crystalline WNPs.

Bright field TEM images of the isolated scheelite $MWO_4$ (M = Ca, Sr, Ba, Pb) WNPs prepared from the SPPT route are shown in Figure 2a–d, respectively. These images reveal that the scheelites formed in TOA/OA vary in size and shape depending on the crystallization temperature and time used. The composition of each scheelite was examined by EDS and confirmed that W was present for each sample along with Ca for (**1** & **2**); Sr (**1** & **8**); Ba (**1** & **7**); and Pb (**1** & **3**). Dark field imaging (see the Supporting Information section) confirmed that the individual scheelite particles were single crystallites.

The bright field TEM image, Figure 2a shows that (**1** & **2**) reacted to synthesize 5 × 15 nm $CaWO_4$ nanorods within 1 min. after reaching the crystallization temperature of 276 °C. The dimensions and uniformity of these rods are in considerable contrast to the reported $CaWO_4$ rods prepared by hydrothermal synthesis using citric acid[49] ( 3–;10 × 31 nm) or CTAB[3] (20–30 × 600–1000 nm), and SOLVO using PEG-200 (20 × 100–250 nm). By switching to (**1** &

NIH-PA Author Manuscript

NIH-PA Author Manuscript

NIH-PA Author Manuscript

**8**) to generate $SrWO_4$, Figure 2b, ~20 nm diamond shaped particles and 5 × 150 nm rods were formed after 2 min. at 367 °C. The inset TEM image in Figure 2b has a 20 nm scale bar and details the edges of the diamonds formed. The reaction between (**1** & **7**) to synthesize $BaWO_4$ at 362 °C for 1 min. formed ~10 nm irregular shaped particles that consist mainly of dots but rough diamond-like structures are also observed, Figure 2c. Using the SPPT route overcomes the limitation of generating these morphologies, within the 20 nm size regime, that have not been reported for SOLVO routes. The dimensions observed for Ba and Sr WNPS prepared by SPPT are of considerable contrast to the micron sized diamond or bi-pyramidal morphologies isolated for $BaWO_4$ and $SrWO_4$ using eggshell membrane templates[5,43] and the block copolymer PEG-b-PMMA in cationic reverse micells.[7]

Finally, $PbWO_4$ produced from (**1** & **3**), contained two morphologies — diamonds and rods — with varying sizes. Figure 2d reveals rods (50–100 nm × 1.0–1.8 μm) while the inset shows an island of diamonds particles (10–50 nm). The differences in shape and size may result from the 15 min. dwell time spent at the crystallization temperature. For example, the middle narrow and crooked wire appears to have been produce by separate diamonds that have oriented themselves and sintered together. A similar oriented attachment process of has been observed for hydrothermally grown $TiO_2$[50] wires and for a wet chemical preparation of (500–800 nm × 3.0– 3.5 μm) $PbWO_4$[8] spindles using cetyltrimethylammonium bromine (CTAB). Based on EDS analysis, both rods and diamonds were assigned to $PbWO_4$.

Overall, the characterization results for the final scheelite nanomaterials indicate that the precursors used in the SPPT route produced WNPs that are fairly uniform, can have narrow size distributions, and possess distinct morphologies that are half to three-quarters smaller than scheelites synthesized from other routes.[4,5,7,8,43] Our synthetic route can produce <30 nm size particles with distinct shapes because: (i) $M(OR)_x$ and $M(NR_2)_x$ precursors are soluble and can easily decompose within the TOA/OA system at relatively low temperatures; and (ii) the SSPT route provides ease of monitoring and adjusting crystallization growth. Overtime, the mixture of $M(OR)_x$ and $M(NR_2)_x$ precursors in the TOA/OA produces rods from attached and oriented diamonds through the Ostwald ripening process.

## SPPT Synthesis of Wolframite WNPs

The SPPT route also was extended to garner a series of wolframite nanorods: $(Mn,Fe)WO_4$ and $MWO_4$ (M = Mn, Fe, Zn) using: (**1**, **4**, & **5**), (**1** & **4**), (**1** & **5**), (**1** & **6**), and (**1** & **9**) respectively. All wolframite reactions were held for 10 min. at specific crystallization temperatures in order to form 1-D $MWO_4$ materials. Figure 3 shows the characterization results for the synthesis of two simple wolframites, $FeWO_4$ and $ZnWO_4$. Using (**1** & **6**) at 330 °C, we were successful in the synthesis of phase pure $FeWO_4$ or ferberite (PDF # 46-1146)[47] 10 × 50 nm rods, Figure 3a. From the reaction between (**1** & **9**) at 340 °C, $ZnWO_4$ or sanmartinite (PDF # 15-0774) nanorods with 10–15 nm diameters and lengths of 60–150 nm were crystallized, Figure 3b. A secondary suboxide $W_{24}O_{68}$ (PDF # 36-0103)[47] phase was also noted in the $ZnWO_4$ diffraction pattern. Through the SPPT route, the aspect ratio of our rods (5–10) are easily formed in 10 min. as compared to 1-D $MWO_4$ prepared from a hydrothermal route that required pH adjustments and 12 h reaction times.[11] The solubility and decomposition of the precursors used also permit isolation of these WNPs in the TOA/OA system.

Next, the synthesis of the solid solution $(Mn_{0.75}Fe_{0.25})WO_4$ and its end members were investigated. Figure 4 and Figure 5 show the TEM, EDS, and PXRD, respectively, for these reaction products. The observed C signal in the EDS spectra is due to a number of sources not directly related to the nanomaterial's C content (e.g., TEM substrate, contamination build-up, differential absorption of the soft carbon X-rays). Figure 4a, shows the bright field TEM image and EDS spectra of nanorods produced from (**1**, **4**, & **5**). The rods produced have ~25 nm diameters, variable lengths of 80–100 nm, and to our surprise, were found to contain Mg, Mn,

NIH-PA Author Manuscript

NIH-PA Author Manuscript

NIH-PA Author Manuscript

Fe, and W. This serendipitous addition of Mg was a result of the incomplete removal of $MgBr_2$ formed during the synthesis of the mesityl precursors. ICP-MS was used to determined the molar ratios of the cations present in the nanorods and found (Mg: Mn: Fe: W) = (0.60: 0.17: 0.26: 1.0). Due to the high Mg concentration and precursor volatility, the PXRD pattern (Figure 5a) for these rods was best identified as a high-temperature (HT) metastable phase of $MgWO_4$ (PDF # 19-0776)[47] known to exist above ~1200 °C.[51–54] Of the alkaline earth tungstates ($A^EWO_4$ where $A^E$= Be, Mg, Ca, Ba, Sr), $MgWO_4$ is known to crystallize in the wolframite structure because of its smaller cationic radii and can crystallize in two polymorphs such as the tetragonal and HT triclinic phases.[53] Our nanorod's diffraction pattern was similar to the pattern for a HT triclinic $MgWO_4$ powder prepared from hydrothermal methods at 210 °C.[51,54] However, the PXRD pattern collected displayed shifted *d*-spacing along with additional allowed reflections. These observations are consistent with the formation of a solid-solution due to the substitution of $Mn^{+2}$ and $Fe^{+2}$ for $Mg^{+2}$. A solid solution containing these cations is not unlikely because the ionic radii are within range (i.e., $Mg^{+2}$ (0.72Å), $Fe^{+2}$ (0.78Å) and $Mn^{+2}$ (0.67Å))[55] to allow for substitution. From our data, we indexed a possible unit cell for the $(Mg_{0.60}Mn_{0.17}Fe_{0.26})WO_4$ nanorods as: orthorhombic, Cmcm , where $a$ = 4.07(1) Å, $b$ = 23.60(1) Å, $c$ = 7.71(1) Å, and V = 741Å$^3$.

Attempts to synthesize the two end members of the targeted binary phase were also performed with separate reactions between (**1** & **4**) or (**1** & **5**). TEM images and EDS spectra for WNPs are shown in Figures 4b & 4c. EDS detected no differences in elemental composition for the mixture of rod-like (10 × 25 nm) and dot-like (10–30 nm) particles formed by (**1** & **4**) which had Mg, Mn, and W (Figure 4b). The primary phase for these WNPs was initially identified as $(Fe,Mn)WO_4$ (PDF # 12-0727)[47] by PXRD. However the absence of Fe presence in the EDS data and confirmation of Mn content suggested the formation of a $(Mg,Mn)WO_4$ solid-solution, with a secondary phase due to the HT $MgWO_4$ phase (PDF # 19-0776)[47,] Figure 5b. The reaction between (**1** & **5**) formed uniform 10 × 80 nm rods with only Fe and W detected, Figure 4c. PXRD indicated multiple phases composed of $FeWO_4$ or ferberite (PDF # 46-1446) [47] along with $Fe_2O_3$ (PDF # 52-1449)[47] and $W_{18}O_{49}$ (PDF # 05-0392)[47] and HT MgWO4 (PDF # 19-0776)[47] Figure 5c. For clarity, a detailed index of the products formed is presented in the Supporting Information.

The formation of $(Mg_{0.60}Mn_{0.17}Fe_{0.26})WO_4$ and the mixed phases observed for $FeWO_4$ and $MnWO_4$ produced from the mestityl derivatives (**4**) and (**5**) suggest that these precursors are highly reactive and capable of forming multiple phases including a metastable HT phase under the conditions used. Further investigations on synthesizing wolframite solid-solutions are currently underway to probe the precursor decomposition pathways[24] and to determine the reaction conditions necessary for isolating the various phases associated with $MgWO_4$. Understanding how to control phase formation of complex solid-solutions and simple systems through the precursor chemistry used is necessary since it is not well understood how all nanostructure-property relationships will deviate from their bulk references. Also as previously discussed, the presence of Mg indicates that Br should be present as the counter anion.[32,33] Because Br was not detected by EDS, it may have reacted in the SPPT system in two different manners. In the first instance, free $H^+$ released either after the coordination of the OA to the nanocrystalline surface or from the reaction of OA with the precursors could lead to the formation of HBr gas. Or Br may have remained in solution and coordinated with a protonated TOA to form $TOA^+Br^-$, which could have been rinsed away with solvents used during the washing process.

## SPPT Synthesis of $W_{18}O_{49}$ Rods

Finally, **1** was was used to explore the precursor influence on the final $WO_x$ phase and morphology produced in the TOA/OA SPPT route. The TEM images, Figure 6a, reveals that

NIH-PA Author Manuscript

NIH-PA Author Manuscript

NIH-PA Author Manuscript

the decomposition reaction of **1** formed single-crystalline nanorods with ~5 nm diameters and lengths of ~100 nm. Two strong reflections (010) and (020) observed in the PXRD pattern, Figure 6b, were indexed to $W_{18}O_{49}$ (PDF # 05-0392)[47] an oxygen deficient $WO_{2.72}$ and intermediate reduction product of $WO_3$.[56] The broadest peaks identified in the pattern were associated with the non-uniform *hkl* line broadening where the *0k0* reflections have sharp peak intensity and the *h* and *l* reflections are broadened. The nanowire's large aspect ratio produces these significant differences in the FWHM values of the peak profiles, as noted for other $W_{18}O_{49}$ nanorods.[19,20] The broadness was not found to be associated with the zero-background sample holder.

The phase and morphology produced from **1** in the TOA/OA system has been reported for other solution[19–21,42] and synthetic routes[56] used to produce nano and micron sized $W_{18}O_{49}$ materials from various tungsten precursors. It can be inferred that any excess $W(OEt)_6$ in the $MWO_4$ reactions could easily form the secondary suboxides phases found in the scheelite and wolframite diffraction patterns. A preliminary investigation of the reaction mechanism for the SPPT route, by FTIR spectroscopy, suggests that $M(OR)_x$ reacts with the OA in the TOA/OA system to produce metal alkoxy acetate species before decomposing into the WNPs. (**1** reacted with OA: CO 1561 $cm^{-1}$ ; neat OA: CO 1710 $cm^{-1}$).[57–61] The formation of a W $(OR)_x(OA)_y$ species in the TOA/OA solvent system is expected, since $M(OR)_x$ readily form complex structures in the presence of carboxylic acids; [57–63] however, due to esterification more complex oxo structures may form as well.[57–63]

## SOLVO Synthesis of WNPs

To demonstrate the versatility of the precursors used to synthesize WNPs, we extended their use to produce $WO_x$ and $MWO_4$ in a SOLVO route using BzOH. Recently, $A^ETiO_3$ nanoparticles were prepared in BzOH SOLVO route from $A^E(ONep)_2$, $A^ETi_2(ONep)_{10}$, Ti $(ONep)_4$ and *in situ* generated "$A^ETi(OCH_2C_6H_5)_6$".[28,64] This non-aqueous system has proven to be an excellent SOLVO route for the general synthesis of metal oxides prepared from M $(OR)_x$ and $M(NR)_x$.

**$WO_3$—**The reaction of **1** in BzOH formed light-blue precipitate that crystallized as a mixture of tungsten oxide $WO_3$ (PDF # 04-005-4487)[47] and tungsten oxide hydrate (*) $WO_3{\cdot}0.33H_2O$ (PDF# 01-087-1203), Figure 7a. Although anhydrous BzOH was used and the reaction was prepared in a glovebox, a secondary hydrated tungsten oxide formed. SEM and TEM images of the precipitate (Figures 7b & 7c, respectively) reveal that $WO_3$ wires with various aspect ratios were produced with lengths up to 10 μm long. This is in contrast to (20–100 × 300–1000 nm) $W_{18}O_{49}$ rods and (30–100 nm) $WO_3{\cdot}H_2O$ platelets, respectively synthesized from $W(OPr^i)_6$ and $WCl_6$ in BzOH at low temperatures and ambient pressure.[27]

**$CaWO_4$—**The reaction between (**1** & **2**) generated 15–40 nm scheelite and $WO_x$ dots, Figure 8 These $CaWO_4$ dots are similar to those prepared from ther SOLVO routes using $Na_2WO_4{\cdot}H_2O$ in ethylene glycol or polyethylene glycol.[1,2] Under the conditions evaluated, the BzOH system does not appear to aid in directing crystalline growth of $CaWO_4$.

Comparison of the SOLVO and SPPT routes show that the two are amenable to $M(OR)_x$, and $M(NR_2)_x$ precursors to yield $WO_x$ and $MWO_4$ particles. However, the SPPT route has an advantage over SOLVO because uniform and shaped particles below 30 nm can easily be garnered in the TOA/OA system. Through SPPT, these previously unattained characteristics of $MWO_4$ can be produced.

NIH-PA Author Manuscript

NIH-PA Author Manuscript

NIH-PA Author Manuscript

## Luminescent Properties of WNPs

Through our synthesis routes, we were able to produce unique WNPs models for an investigation of size and morphology effects on the luminescence behavior.[3,18,20,49] Since previous synthetic routes to $MWO_4$ have been limited in producing uniform <30 nm diamonds and rods, and have not used TOA/OA or BZOH solvent systems, we used this opportunity to measure the photoluminescent (PL) emission of our 15 nm $CaWO_4$ rods and 10 nm $BaWO_4$ diamonds. These particular $MWO_4$ samples have ideal shapes and sizes necessary for alternative bioimaging applications and are being further investigated with lanthanide activators. Measurements of the PL behavior of $W_{18}O_{49}$ rods and 10–30 nm $CaWO_4$ dots were also performed. All particles were washed 3×'s prior to PL characterization. The room temperature PL emission spectra produced for these materials, using $\lambda_{ex}$ = 320 nm, are shown in Figure 9. A vial containing 5 × 15 nm $CaWO_4$ rods dispersed in $CHCl_3$ is shown in Figure 10. Under white light the solution is colorless and under a UV light from a handheld emitter it fluoresces blue. PL investigations on the remaining $MWO_4$ are underway.

The exact mechanism for the optical behavior of $W_{18}O_{49}$ is not well understood since there are few examples of room temperature PL data for $W_{18}O_{49}$ nanomaterials from which to derive information. Multiple emission maxima ($\lambda_{ex}$ = 275 nm) have been previously observed;[20] however, we found that our $W_{18}O_{49}$ nanorods produced only a single broad emission spectrum centered at 430 nm, Figure 9a. Our data was in close agreement with the broad PL emission reported for $WO_3{\cdot}H_2O$ particles centered at 425 nm ($\lambda_{ex}$ = 365 nm).[22] One similarity, to the multiple maximum spectrum reported for other $W_{18}O_{49}$ rods, is that our $\lambda_{em}$ is close to the reported length dependent blue $\lambda_{em}$ = 437 nm ($\lambda_{ex}$ = 275 nm)[20] that increases relative to rod length. The PL behavior of $WO_x$ nanoparticles and rods, in general, has been attributed to result from band-to-band transitions and oxygen defects found at the particle surface. Differences noted may result from the surface moieties and oxygen defects as opposed to the morphology since they are based on particles produced in oleylamine[20] and benzyl alcohol[22], respectively.

The intrinsic luminescence behavior of the $WO_4^-$ for the 15 nm $CaWO_4$ rods, 10–30 nm $CaWO_4$ dots, and 10 nm $BaWO_4$ diamonds was also probed at room temperature using $\lambda_{ex}$ = 320 nm, Figure 9. Similar to $WO_x$ nanomaterials, the effects of size, morphology, and surface chemistry can change the emission behavior of $MWO_4$ nanomaterials. Results for our $MWO_4$ indicate that surface chemistry and particle size have a role in PL intensity and emission behavior. For example, Figures 9b & 9c show the emission spectra for $CaWO_4$ rods and dots, respectively. The broad blue PL emission observed for these $CaWO_4$ rods (from TOA/OA) was centered at 425 nm while the $CaWO_4$ dots (from BzOH) had an emission at 395 nm. The $BaWO_4$ diamonds had an emission at 420 nm, Figure 9d. Despite the morphology and particle size, the PL emission of our 15 nm $CaWO_4$ rods and 10 nm $BaWO_4$ diamonds are within reported ranges for both bulk powders[65] and nanoparticles[2,49] found at 421 and 417 nm ($\lambda_{ex}$ = 290 and 247), respectively. The PL emission maximum, for our 10–30 nm $CaWO_4$ dots, were also within close agreement with films made from $CaWO_4$ dots prepared from reverse micelles ($\lambda_{em}$ = 401 nm, $\lambda_{ex}$ = 240 nm)[65]. Other reports on $CaWO_4$ nanoparticle fluorescence also indicate that particle size and surface chemistry tend to change the intensity and emission maxima.[3,4,49] For example, PL emissions such as 430 nm ($\lambda_{ex}$ = 283 nm)[1], 435 nm ($\lambda_{ex}$ = 238 nm) and 521 nm ($\lambda_{ex}$ = 360 nm)[4] have all been reported for various particle sizes and surface chemistries of $CaWO_4$. In addition, the PL intensity is considered tunable by morphology. Recently, two reports concerning the effects of a critical size and morphology of PL emission behavior of $CaWO_4$ particles have suggested that rods can enhance PL intensity whereas intensity can decrease as a particle size diminishes.[2,49] Overall, broad and weak PL emission demonstrate that our $CaWO_4$ rods and $BaWO_4$ diamonds have low quantum efficiencies, but continue to fluoresce for morphologies in this size regime.

NIH-PA Author Manuscript

NIH-PA Author Manuscript

NIH-PA Author Manuscript

## Summary and Conclusions

We have developed a general SPPT route for the synthesis scheelite, wolframite, and tungsten oxide WNPs which employs, for the first time: $M(OR)_x$, $M(NR_2)_x$, $M(CO)_x$ and $MR_x$. Evaluation of these precursors in the SPPT (triocytlamine/oleic acid) and SOLVO (benzyl alcohol) routes generated as-prepared crystalline products at moderate temperatures that did *not* require further calcination procedures in moderate to high yield. A reduction in crystallization time (minutes) was achieved by precursor selection and the SPPT route, which is in considerable contrast to solvo- or hydrothermal routes which require hours or days. Since the final WNP morphology and size produced by these routes could not be explained by the PSA, the processing conditions for the routes and oriented attachment mechanisms were determined to be the influencing factors. Our experiments did indicate that the SPPT route was successful in generating phase pure, homogenous WNPs with distinct morphologies below <30 nm in size. The final phases of the SPPT derived materials were found to vary based on precursor selection. Phase pure $MWO_4$ particles were produced from an all $M(OR)_x$ route or from the combination of an $M(OR)_x$ with $M(NR_2)_x$ and $M(CO)_x$. For the wolframites, the reactivity and precursor decomposition for the mesityl derivatives allowed the formation of a high-temperature metastable phase of $(Mg_{0.60}Mn_{0.17}Fe_{0.26})WO_4$. Examination of the mesityl derivatives for the synthesis of wolframite end members indicated that their reactivity and decomposition led to mixed phase products. Further evidence for how the reactivity and precursor decomposition influences the phase of the materials produced was also observed for the zinc akyl *neo*-pentoxide (**9**) which formed a mixed phase product versus the alkaline earth *neo*-pentoxides (**7** & **8**) which formed phase pure nanomaterials. Finally, the room temperature photoluminescence was observed using $\lambda_{ex}$ = 320 nm and produced $\lambda_{em}$ = 430, 420, 395, 420 nm for $W_{18}O_{49}$ rods, 15 nm $CaWO_4$ rods, 10–30 nm particles, and 10 nm diamonds $BaWO_4$, respectively. Demonstrating that luminescence of WNPs persists in <30 nm particles with various morphologies

## Supplementary Material

Refer to Web version on PubMed Central for supplementary material.

## Acknowledgments

The authors thank Dr. G. Smolyakov (Center of High Technology Materials) for use of a fluorimeter purchased in part from the NSF IGERT Program on *Integrating Nanotechnology with Cell Biology and Neuroscience* (NSF Grant DGE-0549500), Ms. B. McKenzie (Sandia) and Mr. T. Borek (Sandia) for technical assistance. This work was supported in part by the National Institutes of Health through the NIH Roadmap for Medical Research, Grant #1 R21 EB005365-01. Information on this RFA (Innovation in Molecular Imaging Probes) can be found at http://grants.nih.gov/grants/guide/rfa-files/RFA-RM-04-021.html. This work was also supported by the Office of Basic Energy Sciences at the Department of Energy, and in part by the U.S. Department of Energy. Sandia is a multiprogram laboratory operated by Sandia Corporation, a Lockheed Martin Company, for the U.S. Department of Energy under Contract DE-AC04-94AL85000.

## Reference

1. Chen D, Shen G, Tang K, Zheng H, Qian Y. Mater. Res. Bull 2003;38:1783.
2. Chen S-J, Li J, Chen X-T, Hong J-M, Xue Z, You X-Z. J. Crystal Growth 2003;253:361.
3. Sun L, Cao M, Wang Y, Sun G, Hu C. J. Crystal Growth 2006;289:231.
4. Wang Y, Ma J, Tao J, Zhu X, Zhou J, Zhao Z, Xie L, Tian H. Mater. Lett 2006;60:291.
5. Liu J, Wu Q, Ding Y. Crystal Growth & Design 2005;5:445.
6. Shi H, Qi L, Ma J, Cheng H. J. Am. Chem. Soc 2003;125:3450. [PubMed: 12643705]
7. Shi H, Wang X, Zhao N, Qi L, Ma J. J. Phys. Chem. B 2006;110:748. [PubMed: 16471598]
8. Zhou G, Lu M, Gu F, Xu D, Yuan D. J. Crystal Growth 2005:577.

NIH-PA Author Manuscript NIH-PA Author Manuscript NIH-PA Author Manuscript

9. An C, Tang K, Shen G, Wang C, Qian Y. Mater. Lett 2002;57:565.
10. Lei S, Tang K, Fang Z, Huang Y, Zheng H. Nanotechnology 2005;16:2407.
11. Yu S-H, Liu B, Mo M-S, Huang J-H, Liu X-M, Qian Y-T. Adv. Func. Mater 2003;13:639.
12. Hu X-L, Zhu Y-J. Langmuir 2004;20:1521. [PubMed: 15803744]
13. Huo L, Chu Y. Mater. Lett 2006;60:2675.
14. Geng J, Lv Y, Lu D, Zhu J-J. Nanotechnology 2006;17:2614.
15. Geng J, Zhu J-J, Lu D-J, Chen H-Y. Inorg. Chem 2006;45:8403. [PubMed: 16999440]
16. Chen D, Shen G, Tang K, Liang Z, Zheng H. J. Phys. Chem. B 2004;108:11280.
17. Kloprogge JT, Weier ML, Duong LV, Frost RL. Mater. Chem. Phys 2004;88:438.
18. Ryu JH, Yoon J-W, Shim KB. Solid State Commun 2005;133:657.
19. Woo K, Hong J, Ahn J-P, Park J-K, Kim K-J. Inorg. Chem 2005;44:7171. [PubMed: 16180880]
20. Lee K, Seo WS, Park JT. J. Am. Chem. Soc 2003;125:3408. [PubMed: 12643684]
21. Seo, J-w; Jun, Y-w; Ko, SJ.; Cheon, J. J. Phys. Chem. B 109:5389. [PubMed: 16851566]
22. Niederberger M, Bartl MH, Stucky GD. J. Am. Chem. Soc 2002;124:13642. [PubMed: 12431071]
23. Hernandez-Sanchez BA, Boyle TJ, Lambert TN, Daniel-Taylor SD, Oliver JM, Wilson BS, Lidke DS, Andrews NL. IEEE Trans. NanoBioSci 2006;5:222.
24. Boylle TJ, Hernandez-Sanchez BA, Baros CM, Rodriguez MA, Brewer LN. Chem. Mater 2007;19:2016.
25. Boyle TJ, Bunge SD, Andrews NL, Matzen LE, Sieg K, Rodriguez MA, Headley TJ. Chem. Mater 2004;16:3279.
26. Pol SV, Pol VG, Kessler VG, Seisenbaeva GA, Solovyov LA, Gedanken A. Inorg. Chem 2005;44:9938. [PubMed: 16363865]
27. Polleux J, Gurlo A, Barsan N, Weimar U, Antonietti M, Niederberger M. Angew. Chem. Int. Ed 2006;45:261.
28. Hernandez-Sanchez BA, Boyle TJ, Baros CM, Brewer LN, Headley TJ, Tallant DR, Rodriguez MA, Tuttle BA. Chem. Mater 2007;19:1459.
29. Tesh KF, Burkey DJ, Hanusa TP. J. Am. Chem. Soc 1994;116:2409.
30. Westerhausen M, Schwartz W. Z. Anorg. Allg. Chem 1991;604:127.
31. Gynane MJS, Harris DH, Lappert MF, Power PP, Rividre P, Rividre-Baudet M. J.C.S. Dalton 1997:2004.
32. Solari E, Musso F, Gallo E, Floriani C, Re N, Chiesi-Villa A, Rizzoli C. Organometallics 1996;14:2265.
33. Klose A, Solari E, Floriani C, Chiesi-Villa A, Rizzoli C, Rea N. J. Am. Chem. Soc 1994;116:9123.
34. Boyle TJ, Clem PG, Rodriguez MA, Tuttle BA, Heagy MD. J. Sol-Gel Sci. Tech 1999;16:47.
35. Boyle TJ, Tafoya CJ, Scott BL, Ziller JW. J. Coord. Chem 2000;51:361.
36. Ould-Ely T, Prieto-Centurion D, Kumar A, Guo W, Knowles WV, Asokan S, Wong MS, Rusakova I, Lu¨ttge A, Whitmire KH. Chem. Mater 2006;18:1821.
37. Frey GL, Rothschild A, Sloan J, Rosentsveig R, Popovitz-Biro R, Tenne R. J. Solid State Chem 2001;162:300.
38. Guo DZ, Yu-Zhang K, Gloter A, Zhang GM, Xue ZQ. J. Mater. Res 2004;19:3665.
39. Robbins, M. Fluorescence: Gems and Minerals Under Ultraviolet Light. Phoenix, Az: Geoscience Press, Inc.; 1994.
40. Qu W, Wlodarski W, Meyer Jr-U. Sensors and Actuators B 2000;64:76.
41. Chen S-J, Chen X-T, Xue Z, Zhou J-H, Li J, Hong J-M, You X-Z. J. Mater. Chem 2003;13:1132.
42. Choi HG, Jung YH, Kim DK. J. Am. Ceram. Soc 2005;88:1684.
43. Liu J, Wu Q, Ding Y. J. Crystal Growth 2005;279:410.
44. Zhao X, Li T-k, Xi Y-y, Ng DHL, Yu J. Crystal Growth & Design 2006;6:2210.
45. Park J, An K, Hwang Y, Park J-G, Noh H-J, Kim J-Y, Park J-H, Hwang N-M, Hyeon T. Nature Mater 2004;3:891. [PubMed: 15568032]
46. O'Brien S, Brus L, Murray CB. J. Am. Chem. Soc 2001;123:12085. [PubMed: 11724617]

NIH-PA Author Manuscript

NIH-PA Author Manuscript

NIH-PA Author Manuscript


47. Powder Diffraction file. Newtown Square, PA: ICDD;
48. Hernandez-Sanchez BA, Chang K-S, Scancella MT, Burris JL, Kohli S, Fisher ER, Dorhout PK. Chem. Mater 2005;17:5909.
49. Li L, Su Y, Lia G. Appl. Phys. Lett 2007;90:054105–054103.
50. Penn RL, Banfield JF. Geochimica et Cosmochimica Acta 1999;63:1549.
51. Gunter JR, Amberg M. Solid State lonics 1989;32/33:141.
52. Gunter JR, Dubler E. J. Solid State Chem 1986;65:118.
53. Chang LLY, Scroger MG, Phillips B. J. Am. Ceram. Soc 1966;49:385.
54. Borsch AN, Dorokhov YG, Golub AM. Ukrainskii Khimicheskii Zhurnal 1973;39:724.
55. Shannon RD. Acta. Cryst 1976;A32:751.
56. Pfeifer J, Badaljan E, Tekula-Buxbaum P, Kovfics T, Geszti, Toth AL, Lunk H-J. J. Crystal Growth 1996;169:727.
57. Boyle TJ, Alam TM, Tafoya CJ, Scott BL. Inorg. Chem 1998;37:5588. [PubMed: 11670706]
58. Boyle TJ, Andrews NL, Alam TM, Rodriguez MA, Santana JM, Scott BL. Polyhedron 2002;21:2333.
59. Boyle TJ, Ottley LAM, Rodriguez MA. Polyhedron 2005;24:1727.
60. Boyle TJ, Tribby LJ, Bunge SD. Eur. J. Inorg. Chem 2006:4553.
61. Boyle TJ, Tyner RP, Alam TM, Scott BL, Ziller JW, Potter BG. J. Am. Chem. Soc 1999;121:12104.
62. Chisholm MH, Folting K, Klang JA. Organometallics 1990;9:602.
63. Li X, Xiu-Fen Y. Chin. J. Struct. Chem 1990;9:199.
64. Niederberger M, Garnweitner G, Pinna N, Antonietti M. J. Am. Chem. Soc 2004;126:9120–9126. [PubMed: 15264847]
65. Zhang G, Jia R, Wu Q. Mater. Sci. Eng. B 2006;128:254.

NIH-PA Author Manuscript

NIH-PA Author Manuscript

NIH-PA Author Manuscript

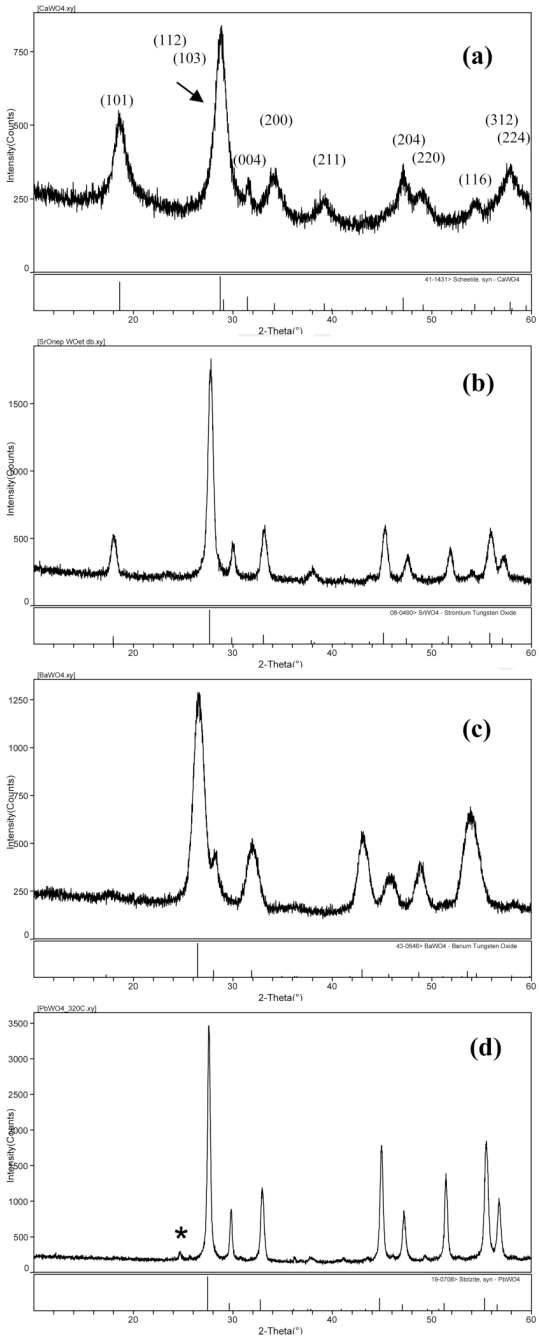


**Figure 1.**

PXRD patterns of scheelite WNPs synthesized from SPPT: (a) **1** & **2** made $CaWO_4$, (b) **1** & **8** made $SrWO_4$, (c) **1** & **7** made $BaWO_4$, and (d) **1** & **3** made $PbWO_4$ and $*W_{24}O_{68}$.

NIH-PA Author Manuscript

NIH-PA Author Manuscript

NIH-PA Author Manuscript

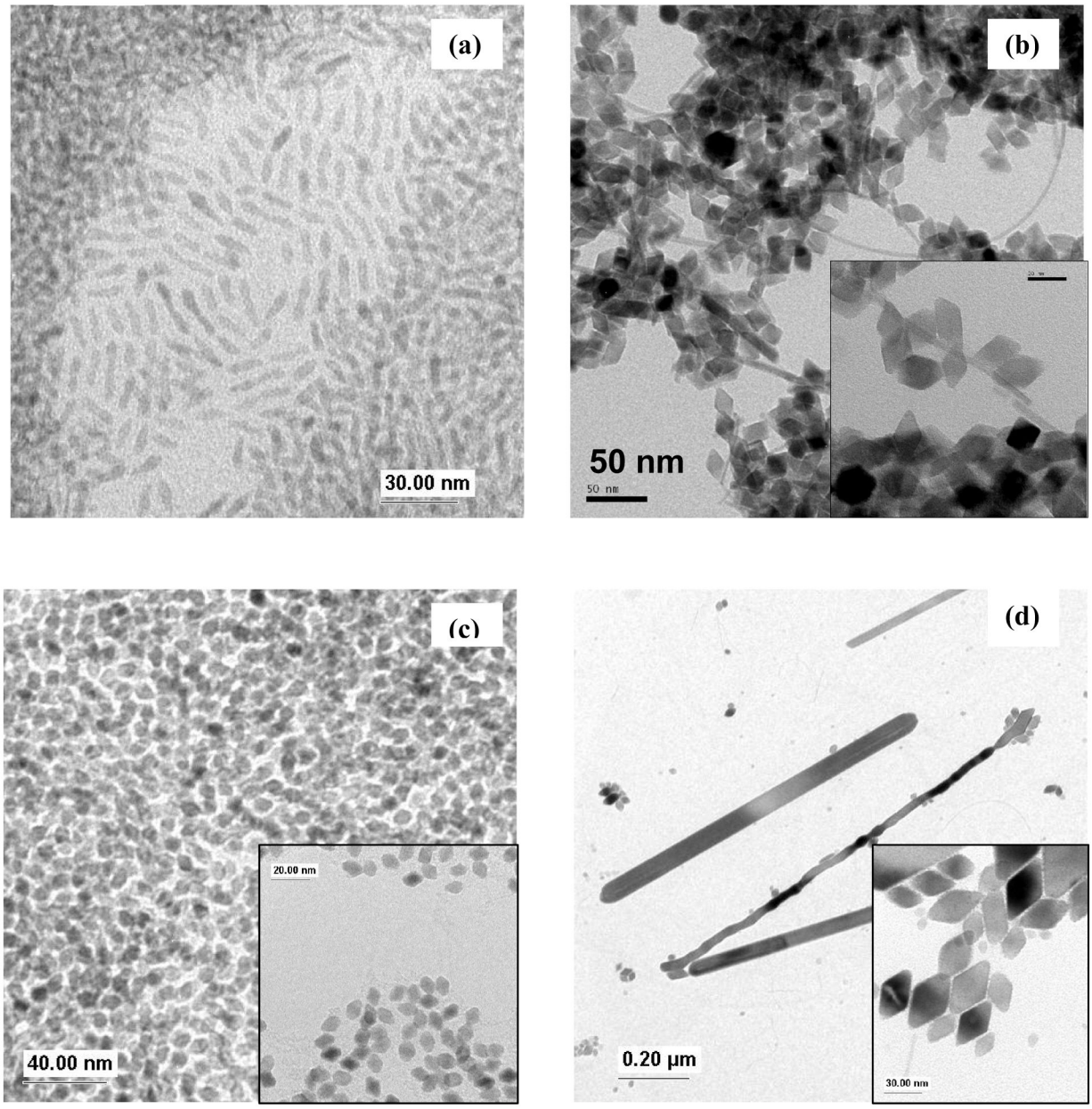


**Figure 2.**
TEM images of scheelite WNPs synthesized from SPPT: (a) $CaWO_4$ (276 °C, 1 min.), (b) $SrWO_4$ (367 °C, 2 min.) inset-20 nm, (c) $BaWO_4$ (362 °C, 1 min.) inset-20 nm, and (d) $PbWO_4$ (356 °C, 15 min.) inset-30 nm.

NIH-PA Author Manuscript

NIH-PA Author Manuscript

NIH-PA Author Manuscript

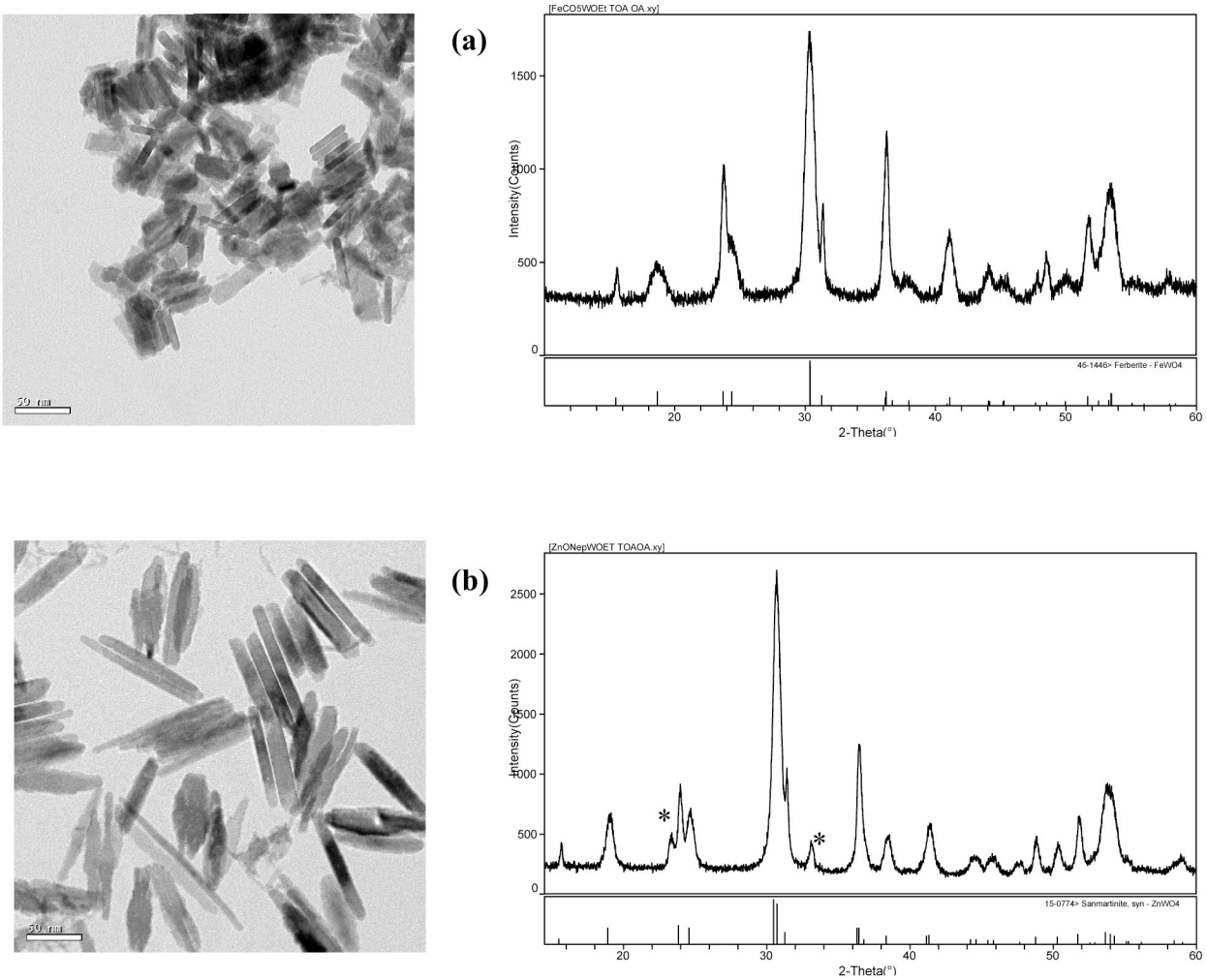


**Figure 3.**

TEM images and respective PXRD patterns for wolframite WNPs synthesized from SPPT: (a) **1** & **6** made $FeWO_4$ (330 °C, 10 min.), and (b) **1** & **9** made $ZnWO_4$ and *$WO_x$ (340 °C, 10 min.).

NIH-PA Author Manuscript

NIH-PA Author Manuscript

NIH-PA Author Manuscript

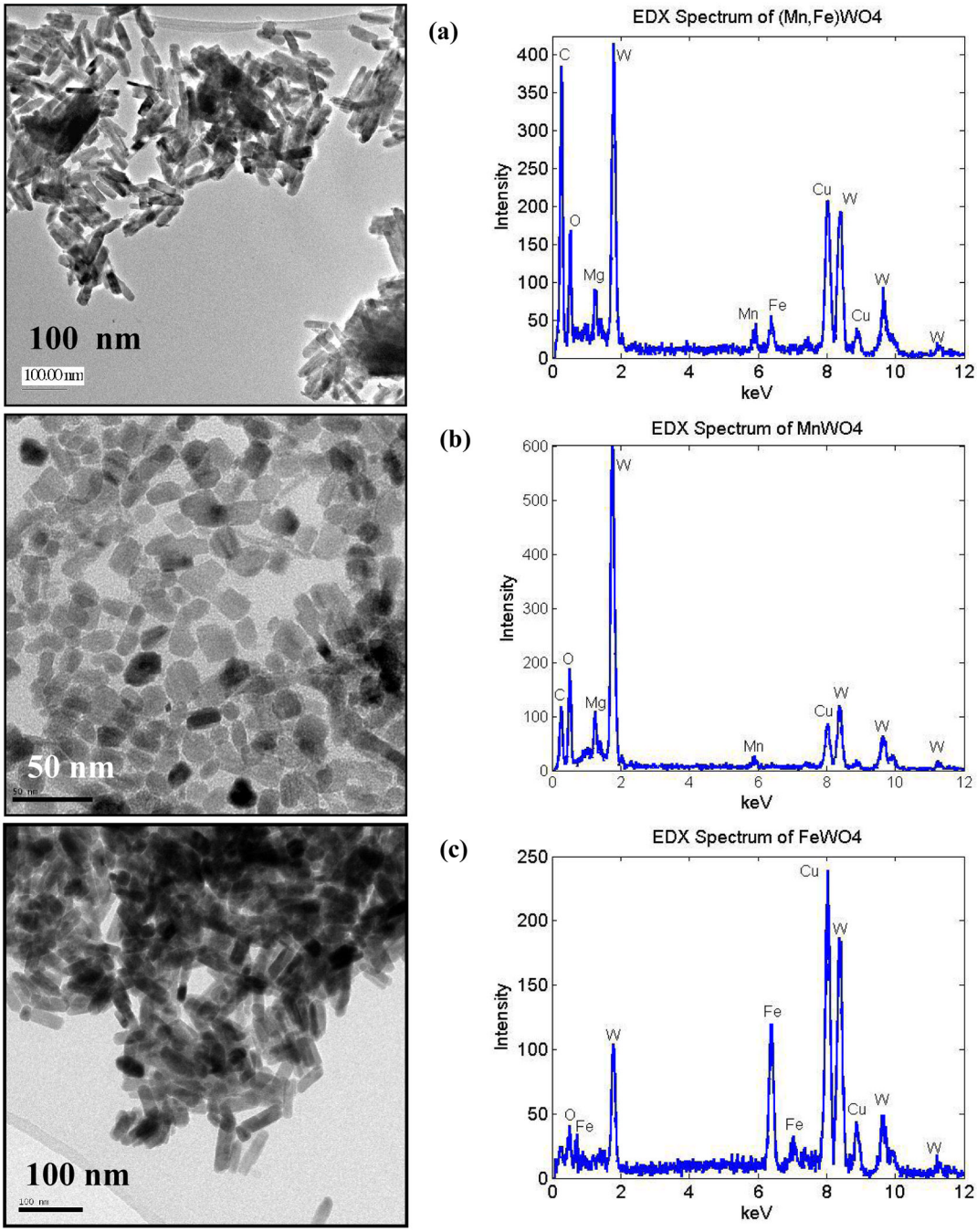


**Figure 4.**

TEM images and respective EDS spectra of wolframite WNPs synthesized from SPPT: (a) $(Mg_{0.60}Mn_{0.17}Fe_{0.26})WO_4$ made from **1**, **4**, & **5** (386 °C, 10 min.), (b) $(Mg,Mn)WO_4$ and $MgWO_4$ made from **1** & **4** (375 °C, 10 min.), (b) $FeWO_4$ and $FeO_x/WO_x$ from **1** & **5** (351 °C, 10 min.).

NIH-PA Author Manuscript

NIH-PA Author Manuscript

NIH-PA Author Manuscript

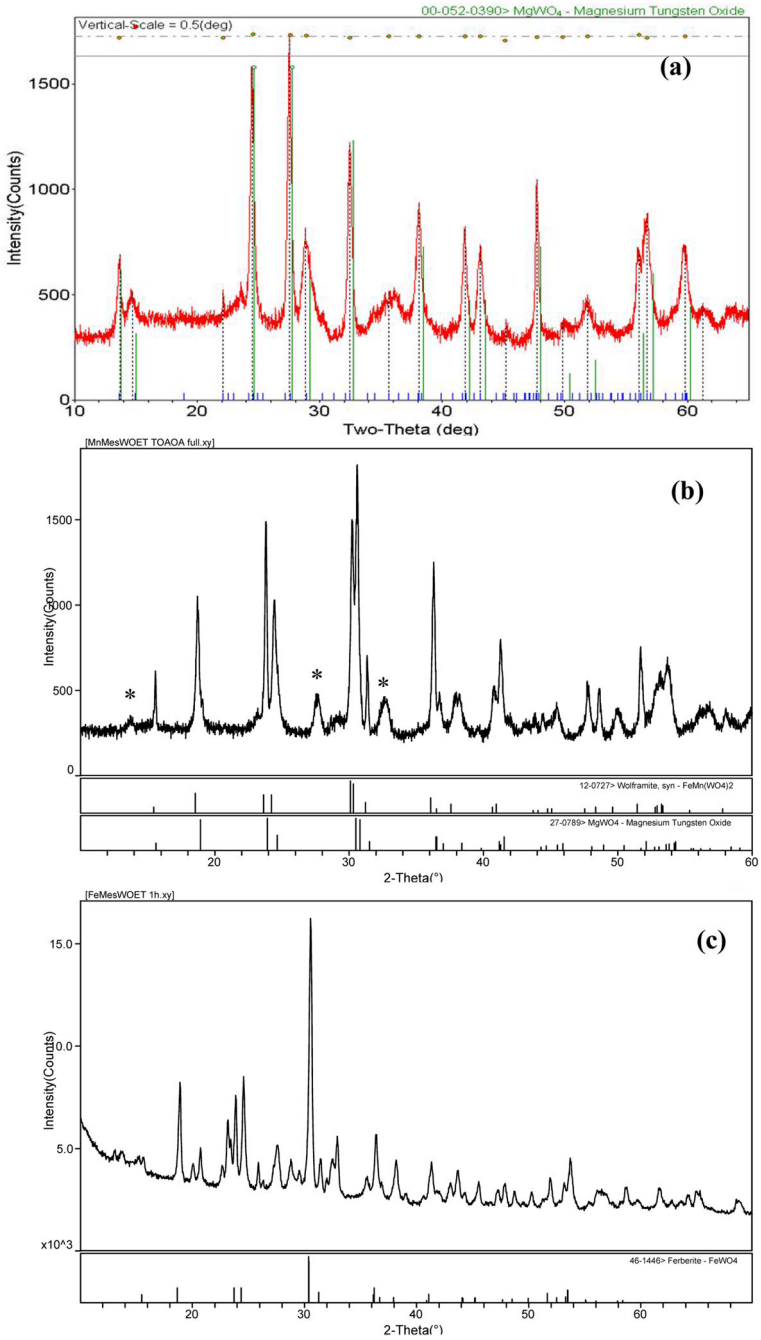


**Figure 5.**

PXRD patterns of wolframite WNPs synthesized from SPPT: (a) **1**, **4** & **5** made $(Mg_{0.60}Mn_{0.17}Fe_{0.26})WO_4$, (b) **1** & **4** made $(Mg,Mn)WO_4$ and *HT $MgWO_4$ (c) **1** & **5** made $FeWO_4$ and $FeO_x/WO_x$ phases.

NIH-PA Author Manuscript

NIH-PA Author Manuscript

NIH-PA Author Manuscript

**(a)**

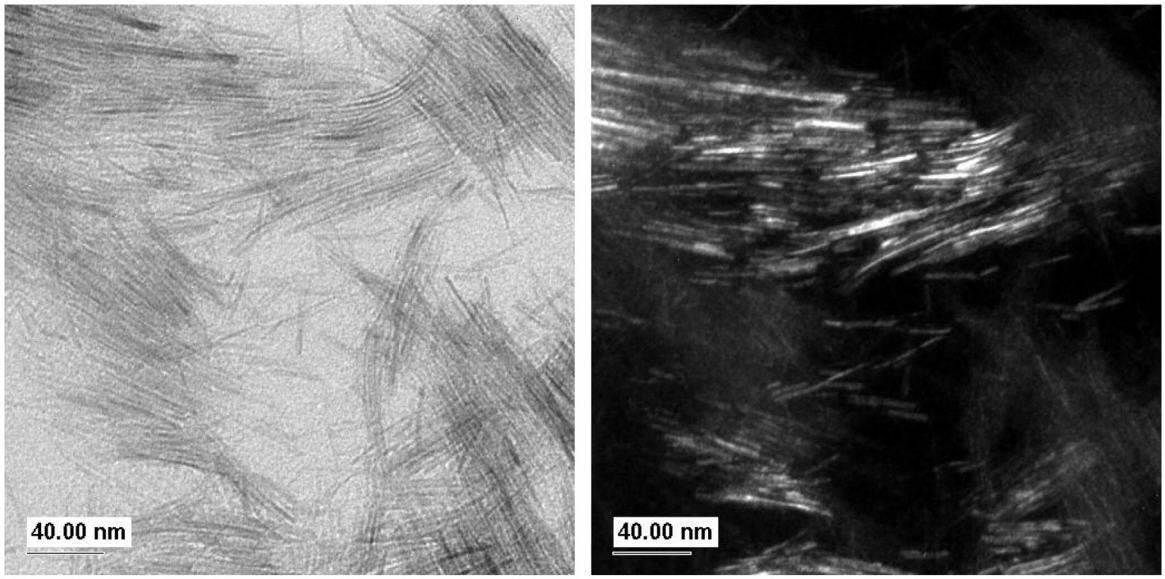


**(b)**

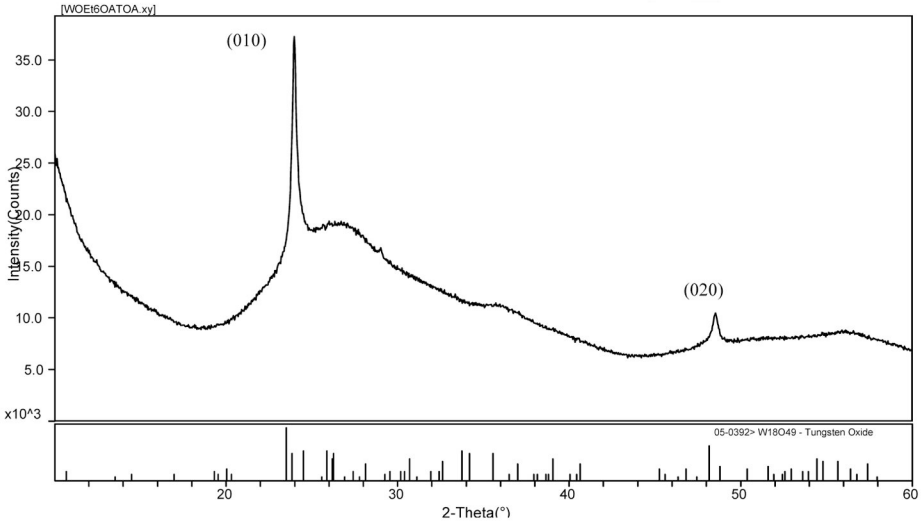


**Figure 6.**

Characterization of $W_{18}O_{49}$ synthesized from **1** using SPPT (310 °C, 10 min.): (a) bright- and dark field TEM images and (b) PXRD pattern.

NIH-PA Author Manuscript

NIH-PA Author Manuscript

NIH-PA Author Manuscript

**(a)**

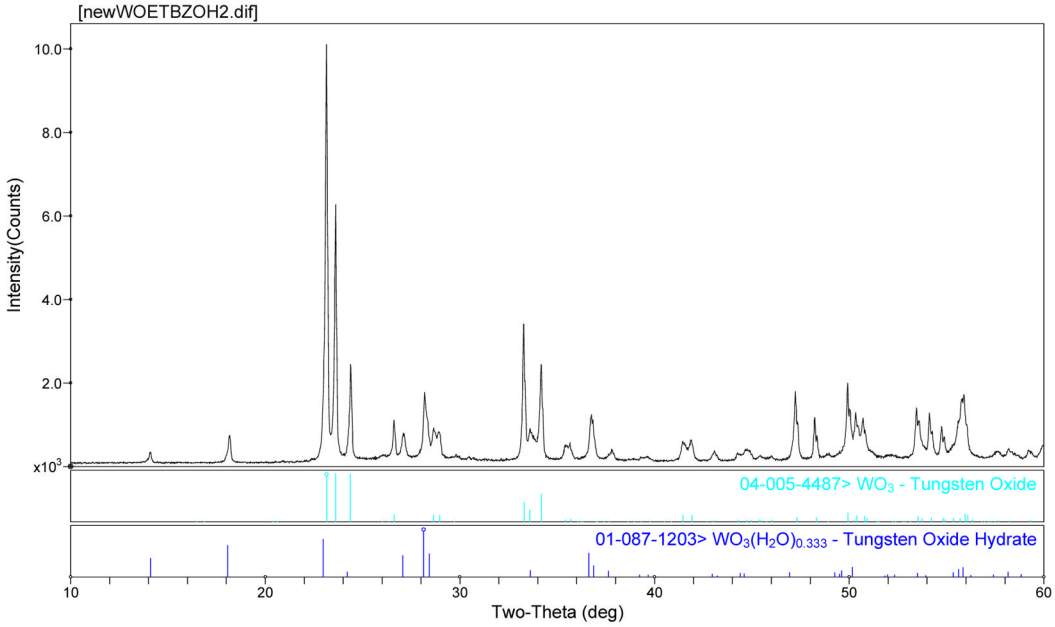


**(b)**

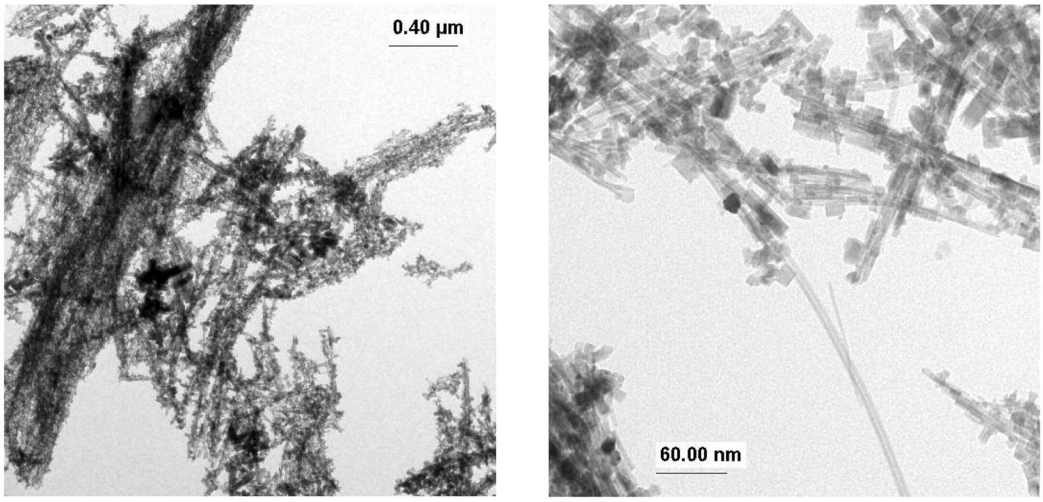

NIH-PA Author Manuscript

NIH-PA Author Manuscript

NIH-PA Author Manuscript

**(c)**

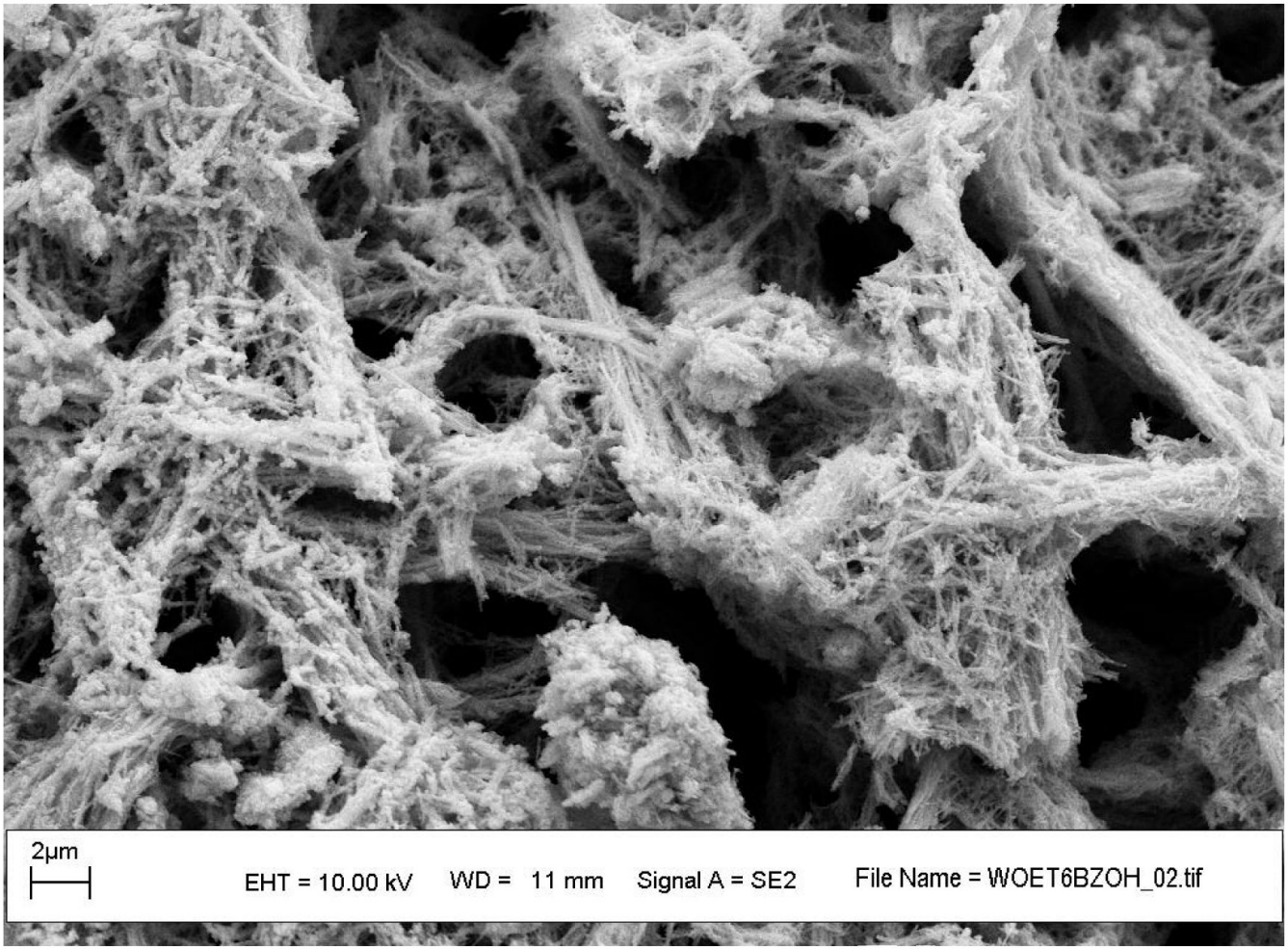


**Figure 7.**

Characterization of $WO_3$ & *$WO_3 \cdot 0.33H_2O$ synthesized from **1** using SOLVO (200 °C, 48 hrs): (a) PXRD, (b) TEM, and (c) SEM image.

NIH-PA Author Manuscript

NIH-PA Author Manuscript

NIH-PA Author Manuscript

**(a)**

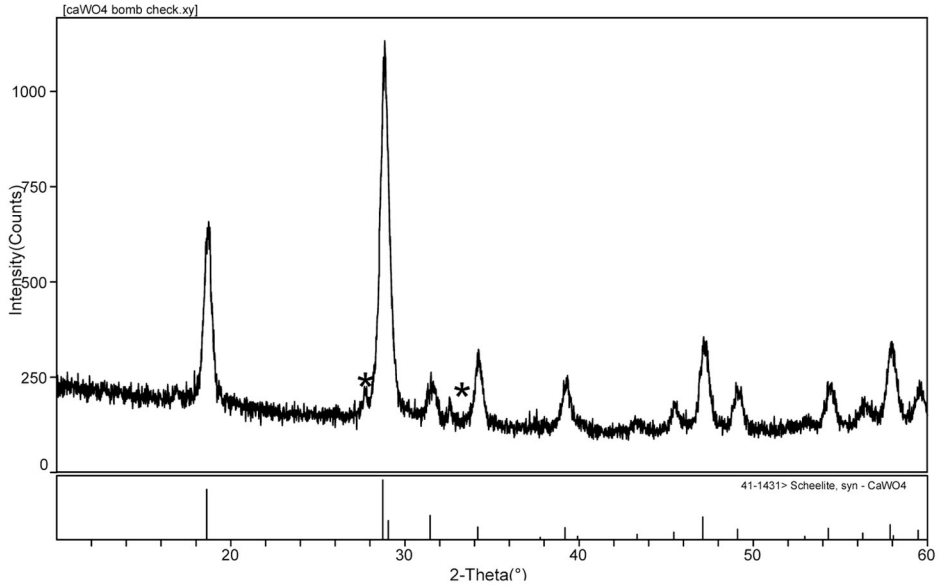


**(b)**

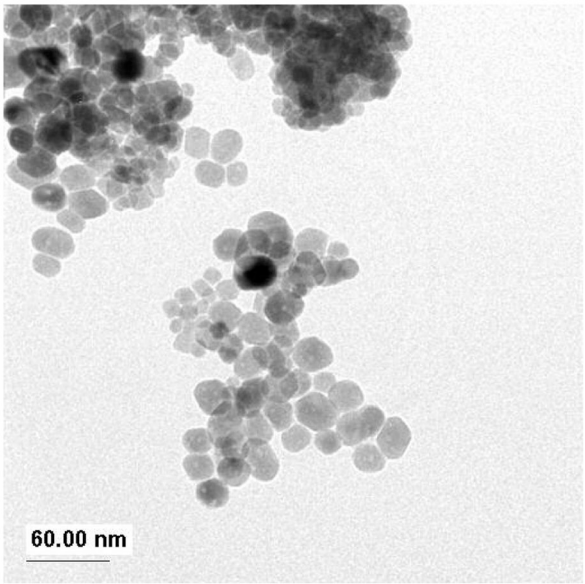


**Figure 8.**

Characterization of $CaWO_4$ and *$WO_x$ synthesized from **1** & **2** using SOLVO (200 °C, 48 hrs): (a) PXRD and (b) TEM.

NIH-PA Author Manuscript

NIH-PA Author Manuscript

NIH-PA Author Manuscript

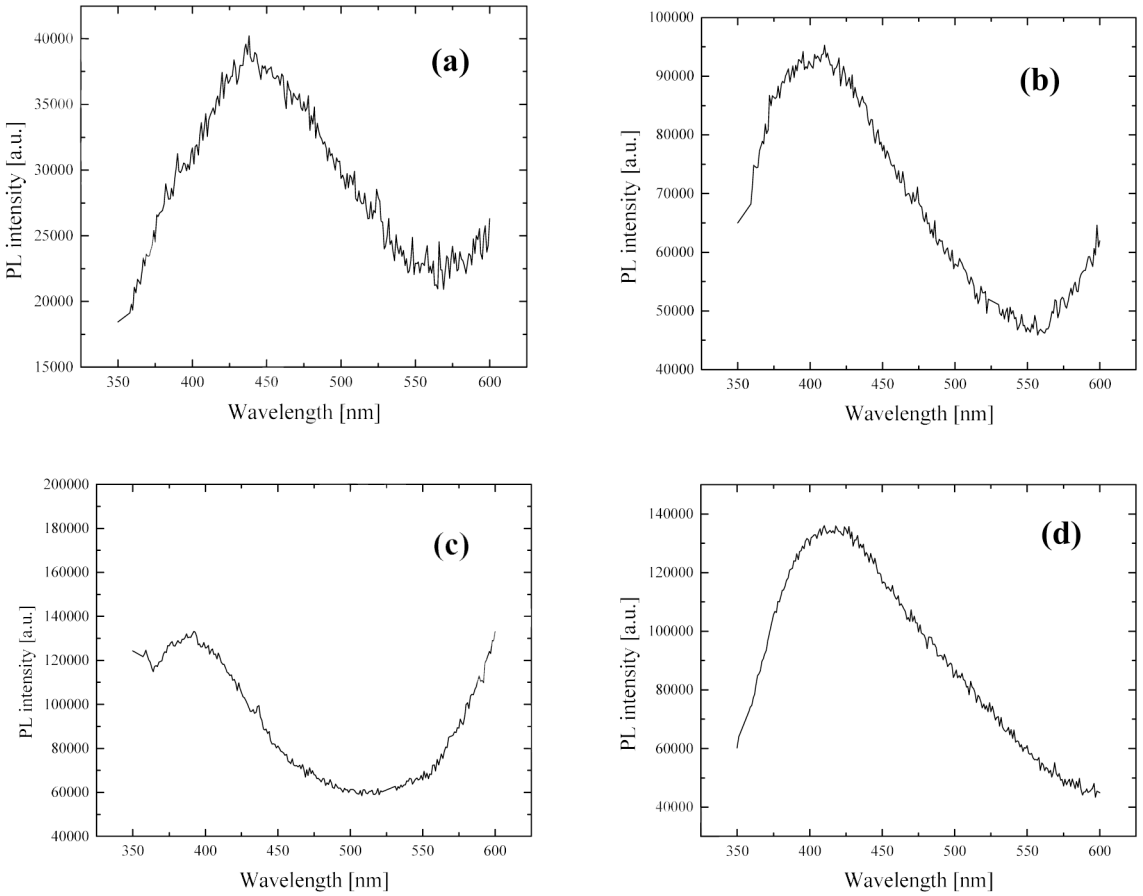


**Figure 9.**

Room temperature PL emission spectra of: (a) 5 × 100 nm $W_{18}O_{49}$ rods, (b) 5 × 15 nm $CaWO_4$ rods, (c) 10 – 30 nm $CaWO_4$ dots, and (d) 10 nm $BaWO_4$ diamonds, $\lambda_{ex}$ = 320 nm.

NIH-PA Author Manuscript

NIH-PA Author Manuscript

NIH-PA Author Manuscript

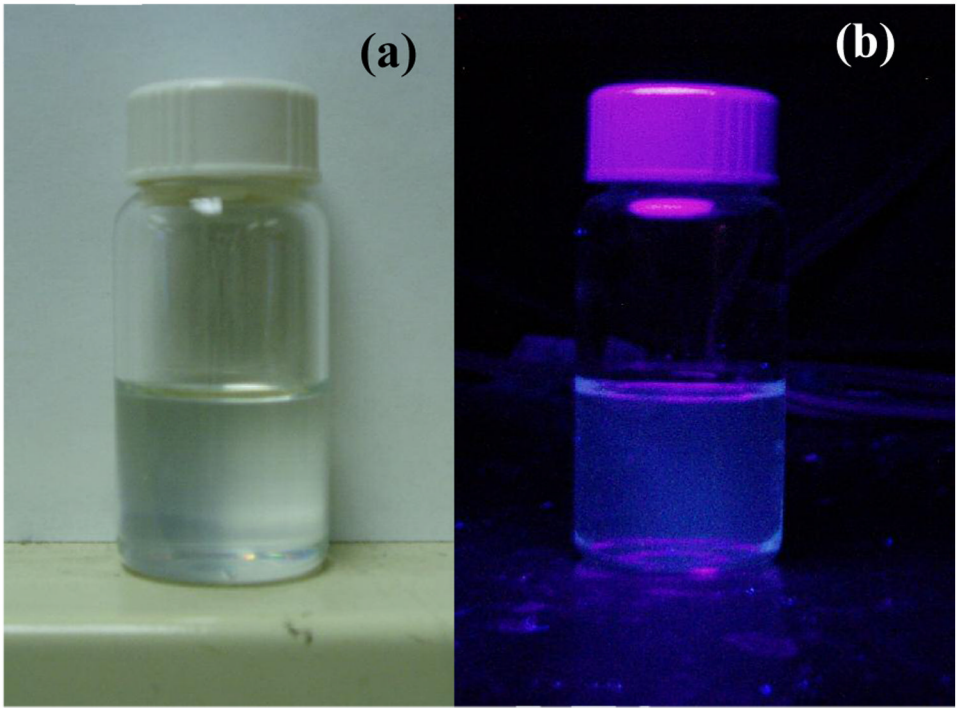


**Figure 10.**
Picture of $CaWO_4$ rods dispersed in $CHCl_3$ under (a) white light and (b) UV light from a handheld emitter.

NIH-PA Author Manuscript NIH-PA Author Manuscript NIH-PA Author Manuscript

**Table 1**

Summary of Reaction Products Formed from SPPT and SOLVO Routes

| Precursor(s) | Reaction | Route | Products | Morphology | Size (nm) | Phase |
|---|---|---|---|---|---|---|
| **1** & **2** | $W(OEt)_6 + M(NR_2)_x$ | SPPT[a] | $CaWO_4$ | rods | 5 × 15 | scheelite |
| **1** & **2** | $W(OEt)_6 + M(NR_2)_x$ | SOLVO[b] | $CaWO_4 + WO_x$ | dots | 15–40 | scheelite mixed |
| **1** & **8** | $W(OEt)_6 + M(OR)_x$ | SPPT | $SrWO_4$ | diamonds & rods | 20 | scheelite |
| **1** & **7** | $W(OEt)_6 + M(OR)_x$ | SPPT | $BaWO_4$ | dots | 10 | scheelite |
| **1** & **3** | $W(OEt)_6 + M(NR_2)_x$ | SPPT | $PbWO_4 + WO_x$ | diamonds & rods | 10–50<br>50 ×1.8 μm | scheelite mixed |
| **1 & 4** | $W(OEt)_6 + M(R)_x$ | SPPT | $(Mg_{0.60}Mn_{0.17}Fe_{0.26})WO_4$ | rods | 5 × 80–100 | wolframite HT-phase |
| **1** & **4** | $W(OEt)_6 + M(R)_x$ | SPPT | $(Mg,Mn)WO_4 + MgWO_4$ | irregular | 10–30 | wolframite mixed |
| **1** & **5** | $W(OEt)_6 + M(R)_x$ | SPPT | $FeWO_4 + FeO_x + WO_x$ | rods | 10 × 80 | wolframite mixed |
| **1** & **6** | $W(OEt)_6 + M(CO)_x$ | SPPT | $FeWO_4$ | rods | 10 × 50 | wolframite |
| **1** & **9** | $W(OEt)_6 + M(OR)(R)_x$ | SPPT | $ZnWO_4 + WO_x$ | rods | 15 × 150 | wolframite mixed |
| **1** | $W(OEt)_6$ | SPPT | $W_{18}O_{49}$ | rods | 5 × 100 | oxide |
| **1** | $W(OEt)_6$ | SOLVO | $WO_3 + WO_3{\cdot}0.33H_2O$ | wires | 10–100 × 10 μm | oxide mixed |

[a] **SPPT:** trioctylamine & oleic acid

[b] **SOLVO:** benzyl alcohol